A novel technique to simulate and characterize a yarn's mechanical behavior based on a geometrical fiber model extracted from micro-CT imaging

Abstract

Textiles and their production machines are increasingly designed using simulations of the textile production process. These simulations require reliable structural yarn models. In practice, these models are often based on simplifying assumptions concerning the underlying geometry. However, in recent years more realistic geometrical fiber models have been developed, but not used to estimate the structural properties of yarns. The current contribution presents a new methodology to obtain a structural yarn model through numerical simulations based on a high-fidelity geometrical yarn model. Starting from microcomputed tomography data of a real-life natural fiber yarn used in air-jet weaving, a geometrical yarn model is constructed by tracing the individual fibers. This geometry is then incorporated in a computational finite element analysis (FEA) framework to obtain the yarn's tensile and bending behavior through a simulated tensile test and Peirce cantilever test. Finally, the results are validated by comparison with experimental data. It is shown that this new technique succeeds to estimate the tensile and bending behavior. The presented methodology allows to gain fundamental insight in the internal deformations and stresses in the yarn. Moreover, it is an important first step toward statistical studies on the structural yarn behavior on the microscale level and towards homogenized macro-models originating from a fully digital workflow.

Keywords

Fiber model, finite element analysis, microcomputed tomography, multi-scale analysis, yarn

1 Introduction

To predict and improve fabric performance and textile production processes, a thorough understanding of the manufacturing process is required. As these processes typically involve complex interactions between multiple moving components, numerical simulations are increasingly adopted. For example, in air-jet weaving, it is crucial to understand the interaction between yarns and air jets to allow for process optimization. To this extent, a numerical framework to simulate the yarn release in the main nozzle of an air jet weaving loom was developed recently[1]. Other interactions occur in tufting, knitting, stitching, and braiding. However, since yarns are an essential component in textile manufacturing, the accuracy of such process simulations depends to a large extent on the employed structural yarn model.

In the past, numerous theoretical structural models were developed that describe the yarn behavior under axial and transversal loading, which is strongly linked to the yarn geometry. To simplify the mathematical derivations, several researchers represented the yarn as an ideal helix[2-6]. This means that each fiber follows a helical path with a constant radius around the yarn axis. Hereby the pitch can be either varying[4] or fixed[5] for different radial layers. In reality however, the yarn geometry is more complex and contains a large degree of irregularity[7]. To overcome these issues, some authors account for this irregularity using distributions of geometrical parameters such as yarn twist, fiber density, and migration[7-12].

In recent years, numerical simulations using finite element analysis have become a new tool to predict yarn behavior. In general, numerical simulations are not restricted by assumptions concerning the geometry to simplify the mathematics, as is the case for theoretical models. This means that real-life yarn geometries can in principle be employed in such simulations. However, researchers still resort to simplified yarn geometries due to the difficulties and high computational cost associated with modeling each fiber individually. For example, the ideal helix representation of the yarn is used in [13-15]. Additionally, Wang and Sun[16] introduced the concept of virtual fibers. Several researchers[17-20] have adopted this strategy to reduce the computational cost since the number of virtual fibers is typically far lower than the number of actual fibers in the yarn, as long as the virtual fiber diameters are adapted so that the cross-sectional area of the virtual yarn matches that of the actual yarn. As such, the number of degrees of freedom can effectively be reduced. In these simulations, which are mainly aimed at technical textiles for composite applications, the yarn is represented as a bundle of straight continuous filament fibers. These idealized geometries differ from real-life yarns where fiber migration occurs, the twist is not constant, packing density varies over the cross-section and fibers have a finite length. Note that it is not straightforward to deal with

staple fibers in these methods[17-20]. As a consequence, actual yarn behavior can still deviate from these numerical predictions[14].

It is clear from the above discussion that current structural models often lack a realistic description of the yarn geometry. However, several authors have attempted to create more reliable geometrical yarn models in the past decade. In the remainder of current work, the terminology geometrical model refers to a model that does not include stiffness or deformation, to distinguish them from the structural models mentioned above. For example, some geometrical models employ a stochastic approach, where the location of fibers in the yarn cross-section is determined by a fiber distribution probability function[21, 22]. Alternatively, Schröder et al.[23] proposed a procedural yarn model with a large number of model parameters that are to be selected manually. To mitigate this manual selection, Zhao et al.[24] proposed an automatic pipeline to estimate these parameters based on microcomputed tomography (µCT) images.

The geometrical yarn models described above are all parametric models. However, it is also possible to consider the full real-life yarn geometry. Indeed, as µCT data contain the volumetric representation of a yarn, it is possible to track individual fibers and as such construct a high-fidelity yarn geometrical model, in contrast to the parametric models described above. Gaiselmann et al.[25] and Huang et al.[26] presented algorithms based on skeletonization that track single fibers in low-density fibrous materials. Recently, Henyš and Čapek[27] extended these algorithms towards yarns, where the fiber contacts are more numerous, challenging the skeletonization.

Despite the progress in geometrical yarn modeling mentioned in the two previous paragraphs, these resulting realistic yarn geometries have to the authors' best knowledge not yet been included in structural simulations to investigate yarn behavior under axial and transverse loading.

This paper aims at connecting the research fields of structural and geometrical yarn modeling. For the first time, a methodology is established that combines high-fidelity geometrical models extracted from µCT images with finite element analysis (FEA) of the structural behavior of staple fiber yarns. This work focuses on a wool-fiber yarn. Inherent to this kind of natural fiber is the increased variability in fiber diameter compared to synthetic fibers, as investigated in e.g. Henyš and Čapek[27]. From the perspective of structural models, the incorporation of staple fibers, fiber migration, and fly-away fibers in a finite element model have to the authors' best knowledge not been done before. Therefore, the new methodology goes beyond existing workflows in order to cope with all the additional challenges mentioned above.

The remainder of this paper is structured as follows. Section 2 explains the workflow, starting with the experimental setup and the validation data (Section 2.1) and followed by the creation of the geometrical model and structural models in Sections 2.2 and 2.3, respectively. Section 3 presents the results of the numerical simulations. In Section 0, the properties of the geometrical model are compared to the available experimental data. The simulation of a tensile test is shown in Section 3.2, together with the sensitivity of the results toward numerical parameters. Section 3.3 deals with the simulation of the Peirce cantilever test and compares the results with the experimental data. Additionally, the flexibility of the current methodology is shown by investigating the influence of yarn twist and inter-fiber friction on the bending stiffness. Finally, the conclusions are presented in Section 4.

2 Methodology

Figure 1 shows the major steps to construct the structural model of the yarn that was investigated by means of finite element analysis (FEA). The following subsections elaborate on each step.

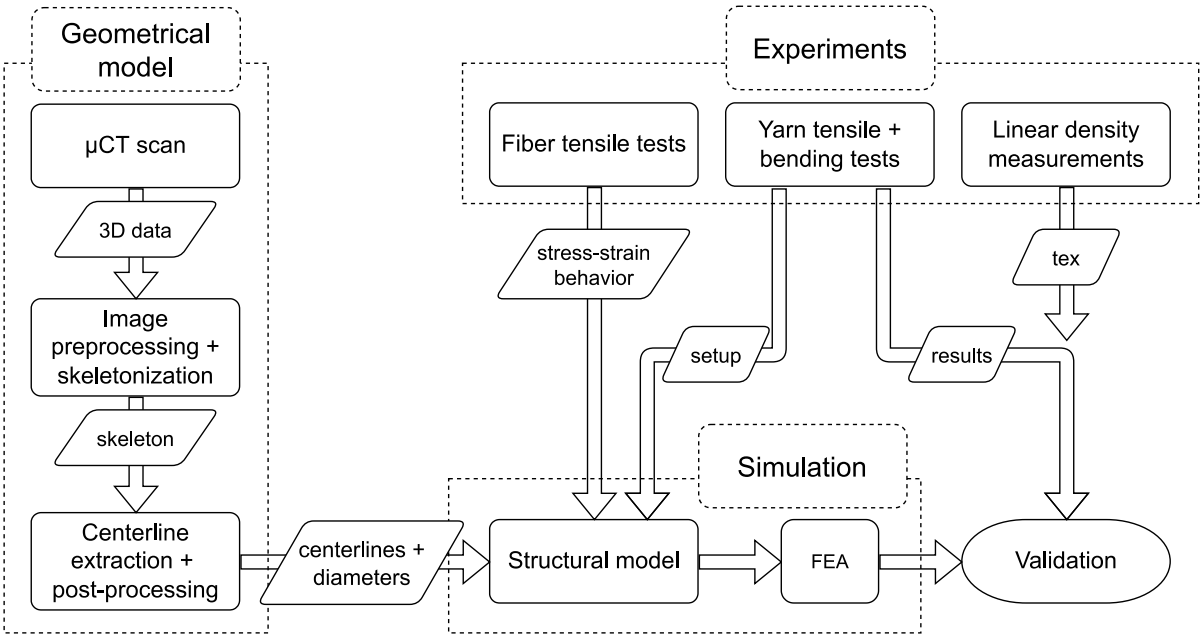

Figure 1 Overview of the methodology.

2.1 Experimental setup and validation data

In this research, a wool fiber yarn, used in air-jet weaving, was investigated. The linear density N was experimentally determined at 28.8 tex $[{}^{g}/_{1000\ m}]$ by weighing a sample of 100 m in length, according to the ISO 2060 (1994) norm.

The tensile behavior of the yarn was experimentally determined using the Textechno Statimat M with a load cell of 10 N. To this extent, 50 samples with a gauge length of 500 mm were given a constant rate of extension of 500 mm/min until breakage. Yarn pretension was set to 0.5 cN/tex. The tensile tests were performed complying with the EN ISO 2062 (2010) norm. The resulting stress-strain curves can be approximated by a piecewise linear function. For the average curve, this results in a Young's modulus of 1.98 GPa ($\pm$0.20 GPa) up to a stress of $60 - 75$ MPa and a modulus of 0.15 GPa ($\pm$0.05 GPa) for higher stresses. The complete stress-strain curves of the yarn samples are shown in Section 3.2, together with the simulation results.

The yarn's bending behavior was determined by means of the Peirce cantilever test[28, 29]. The overhanging length needed for a yarn to reach 41.5° deflection under its own weight was measured for 15 samples. The tests were based on the ASTM D1388-18 standard. However, based on the discussion in Lammens et al.[29], the constant 14.21 has been replaced by the gravitational acceleration, which follows the original formulation by Peirce[28]. The bending stiffness EI is then inferred from

$$EI = N \cdot g \cdot c^3 \tag{1}$$

with

$$c = L \cdot \sqrt[3]{\frac{\cos \theta/2}{8 \tan \theta}} \tag{2}$$

Herein, g is the gravitational acceleration, equal to 9.81 m/s^2, L the measured overhanging length, and θ the deflection angle. For $\theta = 41.5°$, c is approximately equal to $L/2$. The average overhanging length L is found to be 39.85 mm with a standard deviation of 2.72 mm. Consequently, the average bending rigidity EI equals $2.23 \cdot 10^{-9}$ Nm^2 with a standard deviation of $4.96 \cdot 10^{-10}$ Nm^2.

Finally, also the fiber properties were investigated and serve as input to the structural model discussed in Section 2.3. Individual fibers with a sample length of 20 mm were isolated from different locations in the yarn (100 in total). Using the Textechno Favimat with a load cell of 210 cN, the linear density and tensile behavior of these fibers were determined. The test speed and pretension were set to 5 mm/min and 0.80 cN/tex for the linear density test and to 20 mm/min and 1.00 cN/tex for the tensile test, respectively. The fiber tensile tests were carried out according to EN ISO 5079 (2020). The resulting diameter of the fiber is inferred from the measured linear density and the tabulated volumetric density of wool[5] $\left(1310 \frac{kg}{m^3}\right)$ and was found to equal 22.9 µm on

average with a standard deviation of 3.97 µm. The tensile properties are discussed together with the structural model inputs in Section 2.3.

2.2 Geometrical model extraction procedure

The µCT scanning process was performed by RX Solutions, France. For each scan, the machine made three revolutions around the sample, with 1472 images per rotation. The X-ray source was operated with a voltage of 80 kV and a current of 200 mA. Finally, the reconstruction was performed using filtered back projection.

The resulting µCT data consist of 3458 slices of 732 by 919 cubic voxels with an edge length of 1.29852 µm. This leads to a sample length of 4.491 mm along the yarn axis. Each voxel contains an intensity value denoting the attenuation of the X-rays in that region of space. Given a large difference in attenuation for wool compared to the background (air), the wool material can be found using the voxel intensity. The intensity values range between 0 and 60000 with a distribution as shown in Figure 2.

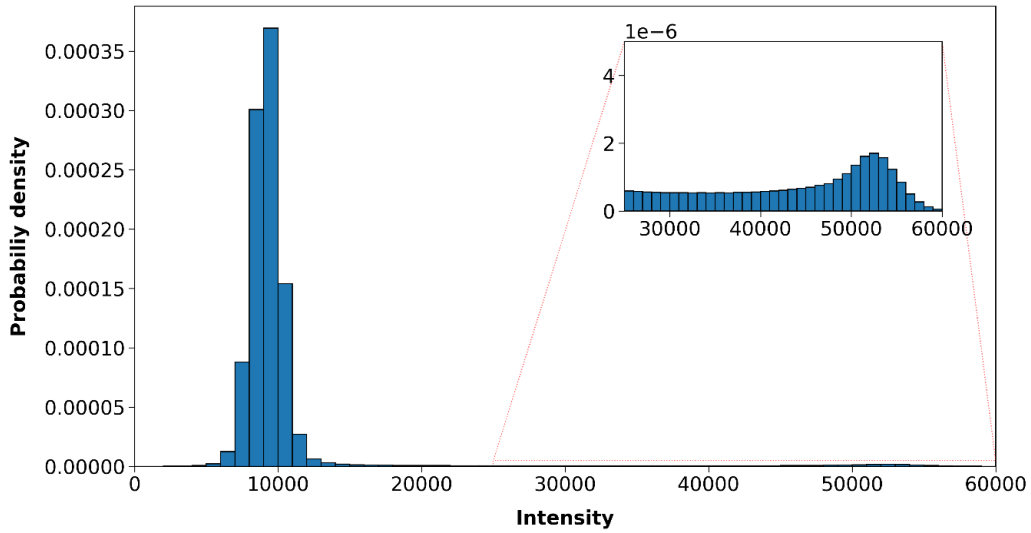

Figure 2 Voxel intensity distribution of the scanned slices. The first (highest) peak corresponds to the background (air), while the second peak (lowest) corresponds to the material (wool fibers). For this distribution, a subset of 35 randomly selected slices (1 % of the total dataset) was investigated.

The geometrical model extraction can be subdivided into three large steps, see also Figure 3. The idea of the procedure is to trace the fiber center lines in the µCT data and consequently reconstruct the fibers as cylinders around these centerlines. The first step, the image preprocessing, deals with the individual slices. The objective here is to separate the fibers from each other, i.e. ‘cutting the bridges’ in the binarized images as illustrated in

Figures Figure 4 and Figure 5, before a 3D skeleton is created using the algorithm of Lee et al.[30]. This skeleton contains centerline fragments. In the second step, the individual fiber centerline fragments are extracted from this 3D skeleton. Finally, these centerline fragments are post-processed. This step includes smoothing the segments, reconnecting the erroneously cut fly-away fibers, removing fibers outside the yarn core, assigning diameters to the segments, aligning the yarn centerline with the z-axis, and avoiding overlap between the fibers. The following paragraphs elaborate on each of these steps.

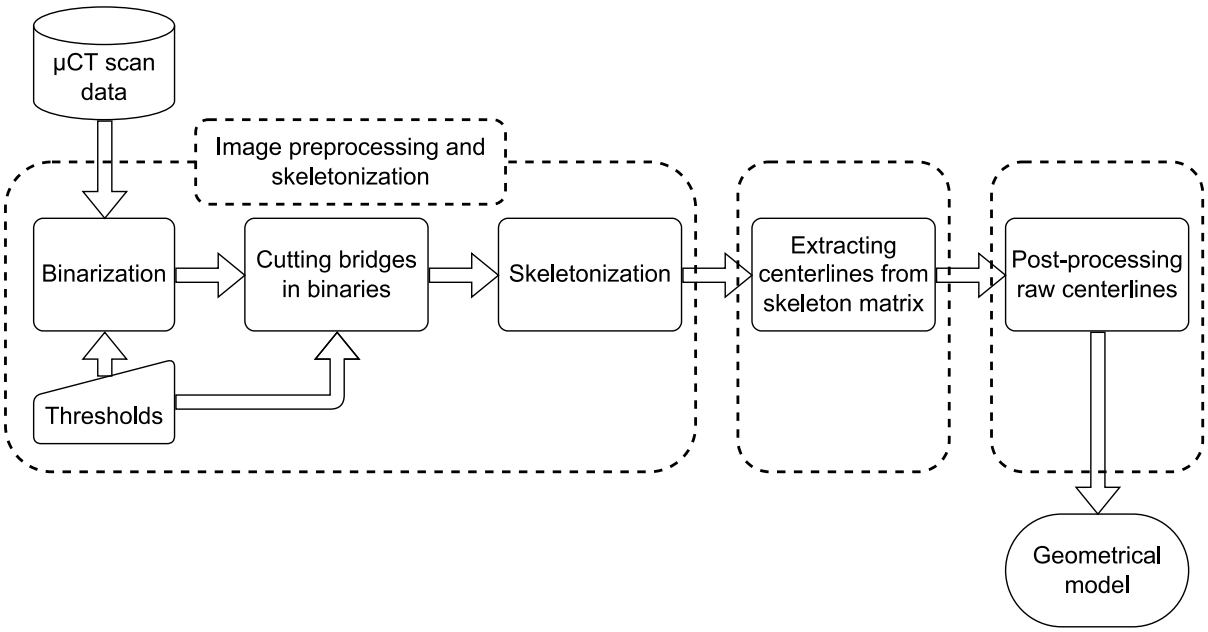

Figure 3 Main steps in the geometrical model extraction process.

2.2.1 Image preprocessing and skeletonization

The main steps of the image preprocessing stage are listed below. Steps 1 – 6 are performed on each slice separately, while the final step consists of recombining all slices to the full volume before performing the skeletonization.

1. Binarize image with intensity threshold T to obtain field B;
2. Construct Euclidean Distance Transform (EDT) of B and as such obtain field D;
3. Apply Gaussian filter on D with standard deviation σ equal to 2 for smoothing, resulting in field $\widetilde{D}$;
4. Identify saddle points and cut bridges from the original binary B to obtain an updated field B_{new};
5. Perform binary erosion of B_{new}. The outer layer of fiber material is removed from the slices, to avoid that material voxels of different fibers touch in subsequent slices;

6. Visual check of modified binaries and if needed, remaining bridges are cut in B_{new};
7. Perform skeletonization on the stack of binary fields B_{new}.

In the first step, each slice is binarized using a high-pass filter, such that each voxel is classified as either air or fiber material. Based on the intensity distribution shown in Figure 2, the threshold T for binarization is selected at 45000 (75% of the maximal values, between the peaks for air and fiber material). As a result of this operation, the binary field B is obtained for each slice. This threshold is much stricter than the one obtained by Otsu's method[31] at 45% of the intensity range. Since the goal of the procedure to create the geometrical model is to represent the fibers by their centerlines, it is not necessary to apply a thresholding technique that captures the fiber surfaces. Capturing the fiber cores suffices. As a benefit, most fibers are already separated in the binary image, in contrast to the binary obtained by the Otsu thresholding. This in turn facilitates the following steps of the image preprocessing algorithm.

If a skeletonization algorithm, such as Lee et al.[30], would immediately be applied to the binarized µCT data, two touching parallel fibers would be considered as part of a single image feature, as also pointed out by other authors[25-27]. As a result, different fibers would be unified. This behavior is evidently unwanted. In literature[25-27], this issue is tackled using Euclidean Distance Transforms (EDT). These EDT maps indicate the minimal distance of a foreground voxel, containing the fiber material, to the background. The EDT map of a yarn cross-section then contains peaks at the fiber center with the magnitude of the fiber radius. This information is then used as input for a second binarization, eliminating the contact regions between touching fibers. In case connected fibers in the skeleton still exist, Gaiselmann et al.[25] developed a stochastic algorithm to cut out regions in the skeleton where fibers touch, and to reconnect these fiber segments afterward based on the distance between the fiber ends and their orientations. This methodology has proven to work for polyester yarns[27].

However, for natural fiber yarns as investigated here, the variability of the fiber diameter is rather large. Indeed, it is found experimentally that the standard deviation of the fiber diameter amounts to 17.5 % of the mean fiber diameter. As a consequence, thresholding the EDT map alone is insufficient since the thickness of the contact region between two large fibers touching might be of the same order as the diameter of a fine fiber. Moreover, due to the dense packing of parallel fibers, the algorithm used by Gaiselmann et al.[25] to cut contact regions from the skeleton and reconnect the segments later on would prove to be difficult due to the numerous contacts and the fact that the difference in orientation of different fiber segments is small.

To alleviate the issues mentioned above, this work proposes a modified approach to cut the bridges that falsely connect neighboring fibers in the binary slices. This approach begins from the observation that in the yarn core, the fibers are more or less perpendicular to the scanned slices. As a consequence, in the EDT map of such a slice, the contact region between touching fibers contains a saddle point. Therefore, the new approach focuses on identifying all saddle points in the EDT of each slice in order to cut the contact region between touching fibers in the binarized image of the said slice. An unwanted side effect of this approach is that fibers running parallel with a slice might also be cut. However, these fibers are exclusively fly-away fibers outside of the yarn core. This means that their impact on the structural properties investigated here is low. Moreover, these fibers are located in areas with low fiber density and can as such be reconnected using the algorithm of Gaiselmann et al.[25].

The above discussion motivates the need for image preprocessing on the slices before performing the skeletonization. First of all, it is necessary to compute the EDT of field B (step 2). Consequently, a smoothing operation, i.e. a Gaussian filter with a standard deviation σ equal to 2, is performed on this resulting EDT map D to reduce the noise, leading to the smooth EDT field $\widetilde{D}$ (step 3). The following paragraphs explain the algorithm to identify saddle points (step 4).

The criteria for the identification of a saddle point are cumulative. Firstly, the voxel must contain material, i.e. $B = 1$. Additionally, one wants to avoid cutting in fiber centers to a maximum extent, therefore the value of D must be below 5.00. This corresponds to approximately 29% of the average fiber diameter. Thirdly, the in-plane components of the gradient of the filtered EDT map, $\widetilde{D}_x$ and $\widetilde{D}_y$, must be small in absolute value. Here, it is chosen that their absolute values are below 0.15 (0.7 % of the average fiber diameter). Finally, according to the second derivative test, the determinant of the Hessian $\mathcal{H}$ of the field $\widetilde{D}$ must be negative: $\det\left[\mathcal{H}\left(\widetilde{D}\right)\right] < 0$.

If all criteria for a certain voxel are fulfilled, the voxel and its 3x3 neighbors (8-neighborhood) are removed from the original binary (B_{new} is set to 0). If the bridge is thick, i.e. the value of the EDT at the location of the saddle point is at least 2.5, then the 5x5 neighbors (24-neighborhood) are cut. Figure 4 shows the identified saddle points as black dots on an EDT map as an example. This saddle point algorithm results in an updated binary field B_{new}. Subsequently, this field is eroded (step 5). This means that from each region of material, the outer ring of material voxels is removed and assigned as background. As such, one avoids that material voxels of different fibers reconnect over different slices.

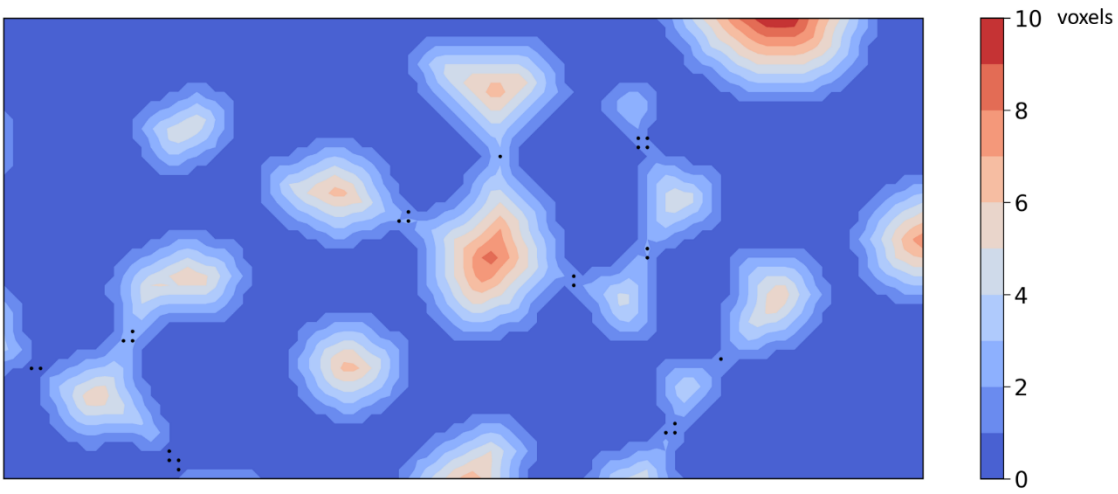

Figure 4 Euclidean Distance Transform (EDT) of a binary slice with the black dots being the identified saddle points. Note that the thickness of some bridges (e.g. left bottom corner) approximates the fiber diameter of the finer fibers (e.g. top right).

An example of the above image preprocessing steps is shown in Figure 5. A visual check (step 6) learns that uncut bridges still exist only in 56 of the 3458 slices (1.6 %), mainly due to violating the second criterion, i.e. the value of D is too high, which means that the bridge is thick compared to the fiber radius. This corresponds to 15 different inter-fiber contact regions as most bridges extend over multiple consequent slices. These remaining connections are cut manually.

Finally, in step 7 the resulting binary slices B_{new} are merged in a single 732x919x3458 matrix and are skeletonized using the algorithm of Lee et al.[30], which reduces the fiber thickness to one voxel as to obtain pseudo-centerline fragments. The image preprocessing algorithm (excluding the manual step 6) takes 153 minutes to complete on the current dataset with an Intel Xeon E5-2680v2 CPU.

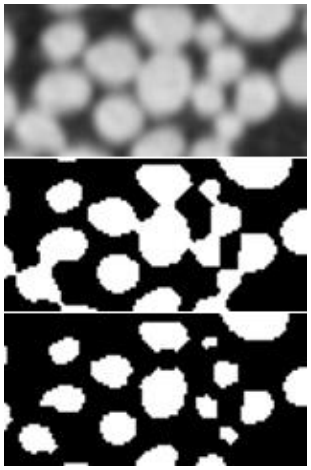

Figure 5 Result of image preprocessing algorithm on a portion of the yarn core. Top: original image; middle: binary obtained by thresholding original image at an intensity of 75 %; bottom: modified binary after automatically identifying and cutting bridges.

2.2.2 Extracting centerlines from the skeleton matrix

The skeleton obtained in the previous section is a single 732x919x3458 matrix in which the material is reduced to a thickness of a single voxel, i.e. pseudo-centerline fragments. The methodology to extract a list of centerlines with the correct connectivity from this matrix is adapted from Nützi[32]. The following paragraphs outline the algorithm.

The goal of this step is to retrieve the fiber centerlines using graphs. The procedure starts from a given voxel in the skeleton matrix that is part of a fiber centerline, a so-called skeleton voxel. Subsequently, all neighboring skeleton voxels in a 3x3x3 or 26-neighborhood of this skeleton voxel are added as a node to the graph, and edge connections between the neighboring skeleton voxels are established. The visited skeleton voxels are then assigned to the background. The walk along this fiber graph is then continued until no further skeleton voxels can be added. This loop is continued for different fiber segments until all skeleton voxels have been visited.

The resulting fiber centerline graphs can still contain branches. Indeed, as the skeletonization procedure aims to conserve the geometrical features, bulges in the binary volume matrix are kept as branches in the graphs. This happens for example due to the image preprocessing and binarization where between slices a sudden change in fiber cross-sectional shape can occur. Moreover, when the saddle point algorithm accidentally removes material from the fiber center, this results in 'needle eyes' in the skeleton. In the current dataset, 0.3 % of the voxels in the skeleton have at least three neighbors and as such are connecting nodes of either branches or needle eyes, which corresponds to 29 % of the centerline graphs. Since the fibers will be represented as smooth cylinders around their

respective centerlines, these branches and needle eyes are obviously unwanted. Therefore, for each fiber graph, the shortest path between all combinations of endpoints in that graph is calculated using Dijkstra's algorithm, and the longest of these paths is selected as the fiber centerline while the other branches are ignored. As a consequence, it is important that no fiber clusters due to uncut connections still exist in the skeleton matrix. If this were the case, unrealistic fibers may be obtained. For example, when two fibers touch each other close to one of the end planes, this is represented by an 'X'-shaped fiber graph. The resulting longest path contains a hairpin turn in that connected region, leading to a 'V'-shaped fiber segment. Moreover, of these two fibers, only one would be retained in the final geometrical model.

As a result of the centerline extraction procedure, 194 fiber segments are found in the used dataset. The calculation time of the algorithm amounts to 86.4 minutes with the main bottleneck being the graph tree building since it includes a point search in a large 3D matrix.

2.2.3 Post-processing raw centerlines

The final stage of the geometrical model creation consists of post-processing the raw fiber centerline segments, and is subdivided into seven steps:

1. Smooth centerline fragments using cubic B-splines;
2. Reconnect erroneously cut fly-away fibers;
3. Remove fibers of other samples, if present;
4. Assign fiber diameters to centerlines;
5. Align yarn axis with z-axis;
6. Prolong fiber ends close to volume boundaries so that the yarn sample ends in a plane;
7. Avoid overlap between fibers.

The following paragraphs motivate and explain each of these steps.

Up until now, all voxel coordinates are integers owing to the discretization of the µCT scan data. Since the voxel length scale is more than 5 % of the average fiber diameter, the resulting centerline paths are too noisy. It is desired to abandon this discretization and represent the fibers in continuous 3D space, with the x and y axes spanning the scan slices and the z-axis normal to the slices. Therefore, as a first step in post-processing, the fiber segments are approximated with cubic B-splines. The smoothing factor s for a segment is chosen to be 1/3 of the number of voxels in that segment. The smoothness of the spline is defined such that

$$\sum_{i=1}^{n} |P_r - P_s|_i^{\,2} \leq s = \frac{n}{3} \tag{3}$$

Herein, n is the number of voxels in the fiber segment, P_r the voxel coordinates of a point on the raw fiber segment and P_s the coordinates of the corresponding point on the spline representation of the fiber segment. In all further postprocessing steps, the fiber segments are represented as discretized versions of these B-splines, with the distance between two subsequent points being 1 µm.

As explained in Section 2.2.1, the saddle point algorithm might also cut in fly-away fibers. Therefore, the second step of the fiber post-processing consists of reconnecting those fly-away fibers. To start, all smoothed fiber segments are inserted in a preliminary list. One by one, a segment is taken and removed from that list. If the first segment end is not too close to the volume boundary (> 20 voxels in the z-direction) and sufficiently parallel to the slice planes (the inner product of the tangent vector with z-axis is smaller than 0.65), this segment end is considered as a candidate for connection and is given index i. The algorithm continues by looping over all other fiber segments j in the preliminary list and the cost function c_{ij}, similar to Gaiselmann et al.[25], is evaluated for this segment pair:

$$c_{ij} = (1 - w)\left(l_{ij} / l_{max}\right)^2 + w\left(\frac{\alpha_i + \alpha_j}{2\alpha_{max}}\right)^2 \tag{4}$$

Herein, w is a weighting factor, set to 0.5, l_{ij} the length of the line connecting the fiber segment ends i and j, l_{max} a maximum length for this connecting line, set to 100 (voxel units), α_i and α_j the angles between the connecting line and the tangents to the segment ends and α_{max} the maximum allowable angle, calculated as $\frac{l_{max} - l_{ij}}{l_{max}} \cdot \alpha$ with α equal to 90°. As such, the maximum allowable angle between the segments and the connecting line becomes smaller with increasing distance between the segment ends. A segment pair is considered a candidate when $l_{ij} \leq l_{max}$, $\alpha_i \leq \alpha_{max}$ and $\alpha_j \leq \alpha_{max}$. The candidate j with the lowest cost c_{ij}, is taken and removed from the preliminary list and added to segment i. This loop is continued until no more candidates can be found. Similar steps are executed for the other end of segment i. Once no more elongations can be made, the elongated fiber segment is stored in the intermediate list. This reconnection procedure reduces the number of fiber segments from 194 to 128.

The following step is particular to the scanning performed in this work. Since two yarns were scanned together, the dataset under investigation also contains fly-away fibers from another yarn sample. These fibers are obviously

unwanted in the final geometrical model. Therefore, a third post-processing step consists of removing these outliers. To identify the outliers, both the yarn axis and its radius must be known. The yarn axis is estimated from the linear regression through all the centers of mass defined on the binary fields B of each slice, see Section 2.2.1. Subsequently, all fibers in the intermediate list are collapsed on a plane perpendicular to this yarn axis, and as such a 2D histogram with a bin size of 5 by 5 voxels is obtained, see Figure 6. The yarn radius is then determined based on the 80 % interval of a normal distribution, being 1.281 times the standard deviation from the center of mass. This procedure is analogous to Zhao et al.[24]. As a result, the yarn radius equals 177.31 µm. Subsequently, for all fibers in the intermediate list, the distance of every point to the yarn axis is determined. A point on a fiber is considered part of the yarn core when this distance is smaller than the yarn radius. If at least 20 % of the fiber's points are within the yarn core and the fiber length is at least 1 mm long, this fiber is retained and stored in the final list. The resulting final list contains 67 fibers after this filtering procedure.

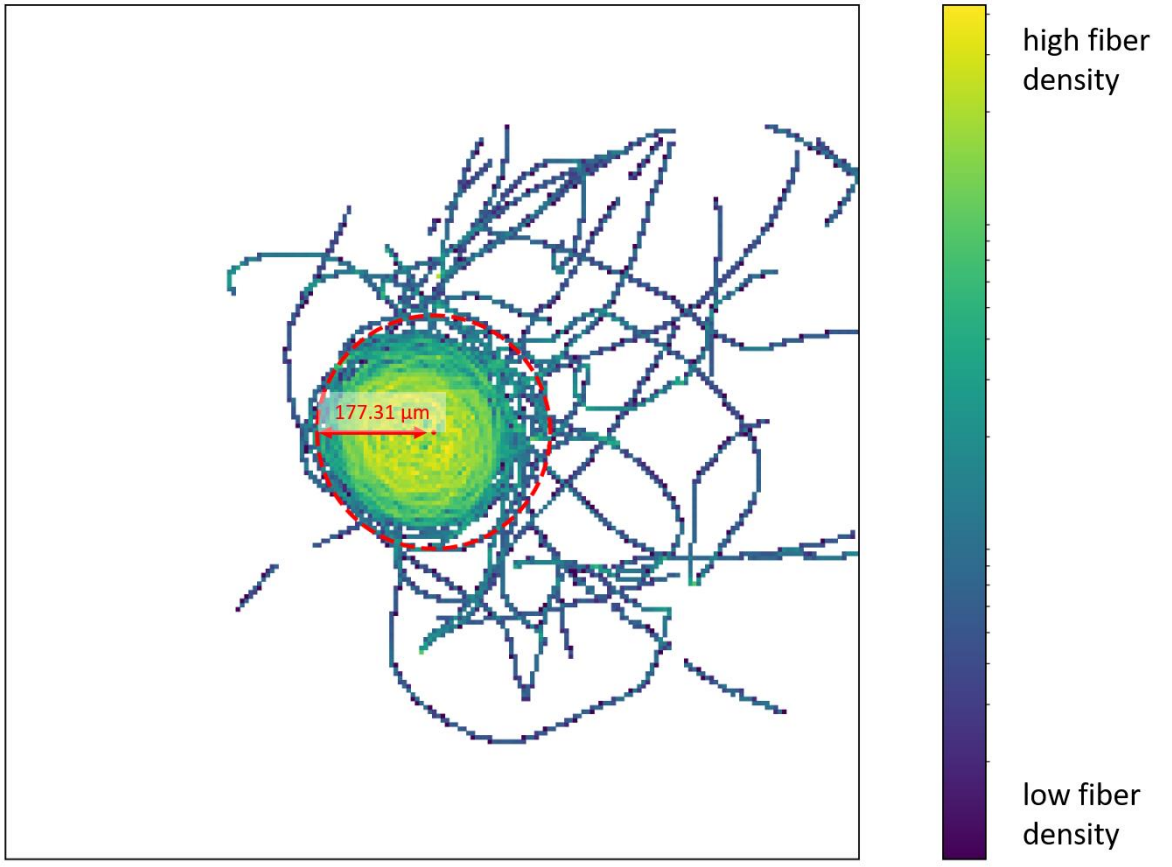

Figure 6 Density distribution of fiber centerlines. The red dot indicates the mass middle point and the dashed circle indicates the envelope of the yarn.

The image preprocessing and skeletonization in fact causes a loss of information about the fiber diameters. Therefore, the fourth step of the fiber post-processing aims to retrieve this information. The procedure is as follows. From all remaining fibers, 5 random points along the fibers are selected given that these points are located within the yarn core. Inside the yarn core, the fibers are oriented more or less normal to the scanned slices. Owing to this orientation, the peak of the EDT in a fiber cross-section is in fact the radius of the maximum inscribed circle and is thus approximately equal to the fiber radius. Therefore, for each of these points, the closest µCT data slice is binarized with a threshold intensity of 30000 (50 % of the maximal intensity), approximating the threshold of 45% of the maximal intensity obtained by Otsu's method[31]. Subsequently, the algorithm searches for the maximum value of the EDT of this binary field in a 9x9 neighborhood of the fiber point under consideration. It is assumed that the fiber radius remains constant over its length and therefore the average of these 5 measurements per fiber is assigned as fiber radius. Since the standard deviation of the fiber diameter along the fiber length appears to be around 6 % of the fiber diameter on average, or 0.9 relative to the voxel size, the assumption of constant diameter along the fiber length is acceptable. In future work, this could be made variable along the fibers. Finally when all fiber radii are known, the approximate linear density of the yarn sample N_{model} is calculated and compared to the experimental value N_{exp}. The fiber radii are then scaled with a factor $\sqrt{N_{exp}/N_{model}}$ in order to obtain the correct linear density in the model.

The fifth step consists of aligning the yarn axis with the z-axis, thus changing from the µCT machine reference frame to the yarn reference frame. This is achieved by translating and rotating the yarn using homogeneous coordinates, a well-known concept in robotics and computer graphics[33]. The translation matrix $\boldsymbol{T}$ follows from the yarn axis start point P_{ys} with coordinates $[x_{ys}, y_{ys}, 0]$:

$$\boldsymbol{T} = \begin{bmatrix} 1 & 0 & 0 & -x_{ys} \\ 0 & 1 & 0 & -y_{ys} \\ 0 & 0 & 1 & 0 \\ 0 & 0 & 0 & 1 \end{bmatrix} \tag{5}$$

Furthermore, the vector $\vec{n}$ is defined as the cross product between the (normalized) yarn axis and the z-axis, and the scalar c equals the dot product between the yarn axis and the z-axis. Then, the matrix $\boldsymbol{N}$ is constructed as

$$\boldsymbol{N} = \begin{bmatrix} 0 & -n_z & n_y \\ n_z & 0 & -n_x \\ -n_y & n_x & 0 \end{bmatrix} \tag{6}$$

Additionally, matrix $\boldsymbol{K}$ is calculated as

$$\boldsymbol{K} = \boldsymbol{I_{3x3}} + \boldsymbol{N} + \frac{1}{1+c}\boldsymbol{N}^2 \tag{7}$$

with $\boldsymbol{I_{3x3}}$ the 3 by 3 identity matrix. Note that c must be different from -1, which is generally the case since the yarn axis is constructed in such a way that its angular deviation with respect to the machine axis is less than 90°. The rotation matrix $\boldsymbol{R}$ equals

$$\boldsymbol{R} = \begin{bmatrix} & \boldsymbol{K} & & 0 \\ & & & 0 \\ & & & 0 \\ 0 & 0 & 0 & 1 \end{bmatrix} \tag{8}$$

Finally, the new homogeneous coordinates are calculated as

$$P_{new} = \begin{bmatrix} x_{new} \\ y_{new} \\ z_{new} \\ 1 \end{bmatrix} = (\boldsymbol{R} \cdot \boldsymbol{T}) \cdot P_{old} \tag{9}$$

for each point.

In the sixth step, the fiber ends near the boundaries of the yarn sample are extrapolated such that their endpoints are as close as possible (within 1 μm) to these boundaries. These extrapolations are small, i.e. less than 1 % of the yarn length, and are caused by both the change of reference frame and the fact that the skeleton of a fiber does not extend entirely to the domain boundaries. Additionally, the units of the coordinates and the fiber radii are converted from voxel coordinates to meters.

Finally, it is verified that the fibers do not overlap. To achieve this, all fiber pairs are compared, each time with one of them called master and the other one slave. The diameter of the master fiber acts as a length scale. Along the master fiber, a walk with steps equal to this length scale is performed. For each of these points encountered in the walk along the master fiber, the closest point of the slave fiber (still discretized with steps of 1 μm) is determined. The distance between the two points is compared to the sum of the fiber radii projected on their connecting line plus 5% of the average of master and slave fiber diameters as margin. If the points are too close, they are both pushed away from each other along the connecting line, each with a magnitude equaling half of the distance deficit. This displacement is then distributed along the fiber length using a Hamming window[34] with the window size being twice the axial length scale. This guarantees that the distance forcing is distributed smoothly over the initial fiber discretization with a spacing of 1 μm. Sharp corners in the fibers are thus naturally avoided. A maximum of 25 iterations is performed, unless the accumulated changes through such iteration loop over all

master fibers drop below 0.01 µm. One iteration takes approximately 2 minutes to complete on the current dataset. After 25 iterations, the accumulated changes have dropped below 0.19 µm.

2.3 Structural models

This Section describes the setup of the structural models for the simulation of both the tensile and bending test, using the geometry derived in the previous section. Since the spatial discretization and material properties are the same for both cases, these are given in the high-level discussion here. The boundary conditions and solution schemes differ for both tests, so these are discussed in Sections 2.3.1 and 2.3.2. All simulations are performed with the explicit solver of Abaqus 2021 (Dassault Systèmes).

The fibers are discretized using linear Timoshenko beam elements (B31) with a spatial resolution of 20 µm along the fiber length, which is in the order of the average fiber diameter, as shown in Figure 7. This results in a mesh of 13737 elements for the complete yarn. The yarn sample in the structural model has a length of 4.491 mm, which is approximately 2.5 twists.

Figure 7 Discretization of the fibers in linear Timoshenko beam elements with a size of 20 µm.

The material properties of wool are based on literature and the fiber tensile tests described in Section 2.1. The volumetric density is set to 1310 kg/m^3, as used in Liu et al.[5]. Since the tensile test considers loading at a constant velocity only and the bending test is in se a case of static loading, the nonlinear viscoelastic behavior of the fibers can be approximated with elastic-plastic behavior. As a consequence, the experimental stress-strain curves are approximated using a piecewise linear fit, see Figure 8, which is represented in the structural model using the elastic-plastic material model provided in Abaqus. Here, the Young's modulus represents the initial (stiffer) linear

region in the measured stress-strain curves of the fibers, and the second linear region of lower stiffness at higher elongations is represented by the plastic part of the model, i.e. a straight line connecting the yield stress with a second stress-strain data point. However, it should be emphasized that no plasticity is expected and that the elastic-plastic model is thus used to capture the purely non-linear visco-elastic behavior. Abaqus assumes constant stress in an element once the plastic strain exceeds that of the last data point given in the material definition. Therefore, this data point is chosen at a high value such that is expected not to be exceeded. Note that breaking of the fibers is not included as this is out of scope of the current work.

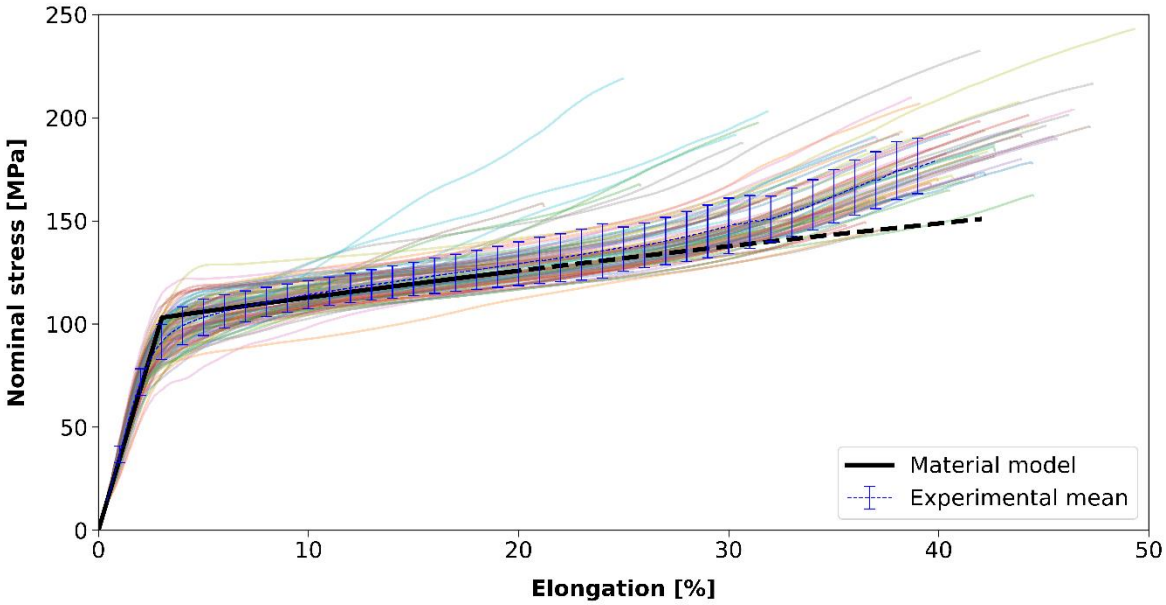

Figure 8 In color, the experimentally measured stress-strain curves of 100 fiber samples on the Textechno Favimat. In blue, the experimental mean curve is given with error bars denoting the standard deviation. In black, the input to the material model is given. The dashed part of the black curve indicates fiber stresses that are in practice not reached in the yarn tensile simulations. For each fiber that fails in the experiments (i.e. when the colored curve stops), the remaining sample size for the calculation of the mean and the standard deviation is reduced.

From Figure 8, one can distinguish three more or less linear regions in the experimental curves, with the stiffness raising again at nominal elongations higher than 30 %. However, in the yarn's tensile simulations, it is observed that these fiber strains are not reached. Therefore, the bilinear approximation is deemed sufficient. Due to the spread of the experimental data, it is not meaningful to define more data points. Based on the experiments, the Young's modulus is set to 3.45 GPa, and the data points $(\sigma_t, \varepsilon_{pl})$ given to Abaqus are $(103.10\ \text{MPa}, 0\ \%)$ and $(258.10\ \text{MPa}, 100\ \%)$, respectively. The plastic strain ε_{pl} is computed as

$$\varepsilon_{pl} = \varepsilon_t - {}^{\sigma_t}/_{E} \tag{10}$$

with $(\sigma_t, \varepsilon_t)$ the data couple obtained from the Favimat data (true stress and strain) and E the Young's modulus. The fiber cross-section remains constant during the simulation, as such the nominal stresses are equal to the true stresses. The shear modulus of the wool material G is set to 1.5 GPa, based on Hearle[35].

Another important material property is the inter-fiber friction coefficient. In Hearle[35], the values range between 0.13 and 0.61 for the static friction coefficient between wool fibers, depending on the directionality of the scales. Moreover, it is postulated[35] that Amontons' law does not hold strictly, meaning that the friction coefficient is not independent of the load. For sake of simplicity, this is still assumed true in current simulations and a fixed friction coefficient of 0.25 is opted for. The sensitivity of the results towards this value is verified later on, see Section 3.3.

In order to recognize the inter-fiber contacts, Abaqus' general contact algorithm is enabled, which uses the penalty method to enforce the contact constraints. To reduce the contact penetration in the tensile test, the default penalty coefficient is scaled with a factor of 10. The critical contact damping fraction is set to 0.5. Other settings keep their default values.

Finally, some material damping is added to the model to remove low-frequent oscillations. To this extent, Rayleigh damping is enabled:

$$\alpha = {}^{4\pi}/_{T} \tag{11}$$

with α the mass proportional Rayleigh damping and T the observed vibration period. The stiffness proportional Rayleigh damping is disabled due to its adverse impact on the stable time increment. A preliminary bending simulation without material damping revealed a vibration period of about 4.15 ms, which is considered as a characteristic time unit for the simulations in the remainder of this work. Therefore α is set to 3028 s^{-1}. The same damping value is used in the tensile simulations. However, it has to be verified that this does not induce additional reaction forces. To analyze the effect of this parameter, its value has been decreased by a factor of 10 and it was observed that the resulting stress-strain curve shows a similar behavior, albeit noisier. Increasing the damping with a factor of 10 leads to a stress-strain curve that is shifted upwards, indicating that this higher material damping induces an unphysical reaction force in the material.

2.3.1 Tensile test

The boundary conditions are applied to two reference points which are defined at the ends of the yarn axis. A kinematic coupling constraining all but the radial direction between the reference points and fiber ends close enough to the reference points, i.e. less than 2.5 % of the yarn length, ensures that the boundary conditions are transmitted to the fibers. The idea is that when this radial movement with respect to the yarn axis is allowed, the yarn sample will contract as if it were part of a longer sample. The yarn start reference point, with z-coordinate 0, is clamped and the end reference point, with z-coordinate equaling the yarn length, is given a constant axial velocity of $v = 500\ \mathrm{mm/min}$, equaling the test speed of the experiments.

As a solution scheme, the explicit central difference time stepping method is opted for to solve the contacts in a computationally beneficial manner. Uniform variable mass scaling is enabled such that the stable timestep size is increased to 10^{-7} s, allowing for a faster simulation. The mass scaling factor is updated every time step. The simulated time is chosen such that the elongation of the yarn reaches 15 % at the end of the simulation. It is set to $0.081\ s$.

2.3.2 Bending test

The kinematic coupling between the reference points and fiber ends is similar to those in the tensile test. However, now also the radial direction of the fiber ends at the yarn start, with axial coordinate 0, is constrained. This reference point is clamped, the other reference point is free to move and rotate in all directions. However, since the modeled sample is only a fraction of the experimental samples, a concentrated force and moment are applied to this free end such that an equivalent overhanging length similar to the experiments is observed:

$$F_y = -w \cdot g \cdot (L - l) = -9.17 \cdot 10^{-6}\ \mathrm{N} \tag{12}$$

$$M_x = w \cdot g \cdot \frac{(L - l)^2}{2} = 1.63 \cdot 10^{-7}\ \mathrm{Nm} \tag{13}$$

with w the yarn mass per unit length, g the gravitational acceleration, L the average experimental yarn length (40 mm), and l the length of the yarn model. Due to the kinematic coupling, the yarn end remains planar, albeit not necessarily normal to the yarn axis, and radial contraction is possible. Gravity is enabled with $g = 9.81\ {}^{\mathrm{m}}/_{\mathrm{s}^2}$ in the negative y-direction.

The time stepping scheme is once more explicit, but in this simulation, no mass scaling is enabled since the addition of mass scaling would lead to a higher oscillation period of the yarn such that the total simulation time would have to increase proportionally. In other words, there is no gain from choosing larger stable timesteps. The loads, both gravity and the concentrated loads, are applied using a smooth step such that the structure experiences the full load after the characteristic time unit T, equal to 4.15 ms. The first and second derivatives of this smooth step function are zero at $t = 0$ and $t = 4.15$ ms. The simulated time is chosen equal to twice the characteristic time unit, or 8.30 ms, as to obtain a steady-state solution.

3 Results and discussion

The results are structured as follows. In Section 3.1, the geometrical model obtained by the procedure described in Section 2.2 is discussed and matched with the µCT images. Moreover, the fiber diameter distribution of the model is compared to the experimental samples of the fiber tensile test. In Section 3.2, the simulation of a yarn's tensile test is discussed. Firstly, the obtained stress-strain curve of the yarn is validated with the experimental measurements. Secondly, the advantage of the proposed digital workflow is illustrated by showing internal stress distributions in the yarn on the fiber level. Finally, the sensitivity of the simulation toward numerical parameters is evaluated. At last, Section 3.3 deals with the simulation of the Peirce cantilever test. After the validation of the results, the influence of some physical parameters, i.e. the yarn twist and inter-fiber friction coefficient, is discussed, again proving the versatility of the proposed methodology.

3.1 Geometrical model

The resulting yarn geometry, including two slices of the µCT scan data (in grey), is shown in Figure 9. It is clear that the proposed methodology succeeds in creating a high-fidelity geometrical yarn model based on µCT scans.

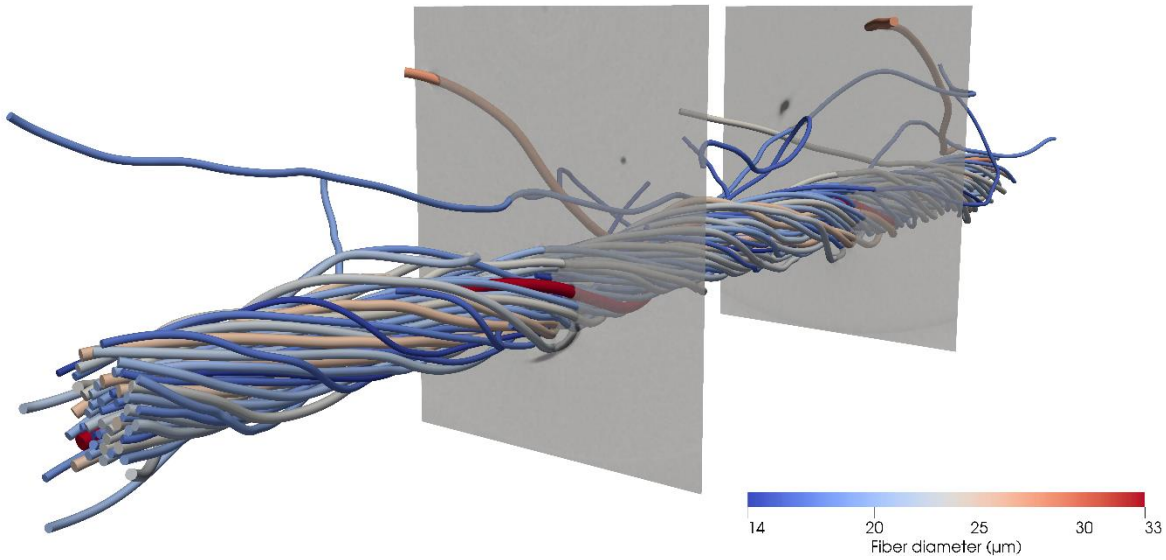

Figure 9 Resulting high-fidelity geometrical yarn model. The fibers are colored by diameter. The grey planes are slices of the µCT scans. The modeled fibers overlap so well with their counterparts in the scanned data that the fiber cross-sections in the slices are practically hidden, indicating a good correspondence between the model and the scanned data. The extracted geometrical model has a length of 4.491 *mm.*

The diameters of the 67 fibers in the geometrical model and those inferred from the linear density measurements on the Favimat (100 samples) are compared using the histogram in Figure 10. It can be seen that the average fiber diameters μ and their standard deviation σ correspond well. The structural Abaqus model has a linear density of 27.4 tex, which is 4.9 % lower than the experimental value of 28.8 tex. The reason for this difference is three-fold. Firstly, in the centerline postprocessing, the fiber diameters are rounded down to the nearest integer µm, and fibers shorter than 1 mm are not considered in the geometrical model. Secondly, a theoretical volumetric density is used in this work, which depends on the moisture content. Since the lab conditions for the experimental linear density measurements on the Textechno Favimat differ from the conditions in the µCT scan, this can influence the results. Finally, the discretization in Abaqus differs from the discretization performed in the centerline postprocessing as the former uses an element size of 20 µm and the latter considers a spacing of 1 µm between subsequent points. Considering these differences, the agreement between the obtained geometry and the experiments is excellent.

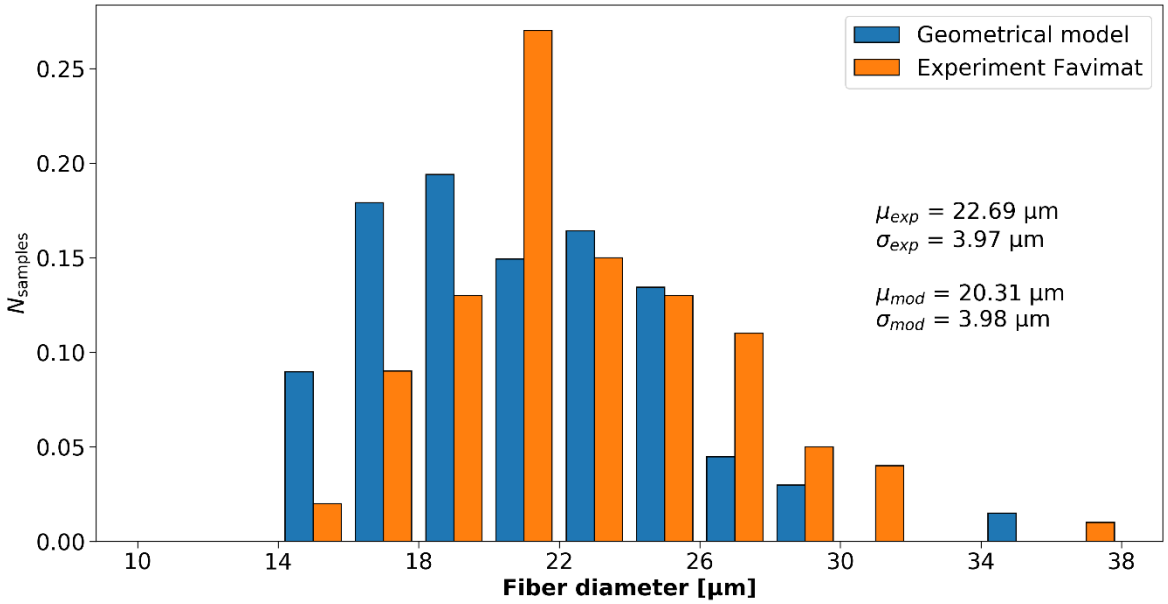

Figure 10 Comparison of fiber diameters in the geometrical model with those tested in the Textechno Favimat. The subscript 'exp' denotes the experimental values and 'mod' those from the geometrical model. The number of samples in each bin is divided by the total number of samples in the experiment (100) or the model (67).

3.2 Simulating a yarn's tensile test

The stress-strain behavior of the yarn model is compared to the experimental results in Figure 11. The simulated yarn stress is computed from the reaction force in the displaced reference point using the modeled yarn count, 27.4 tex. It can be seen that the simulated curve fits well in the experimental data, proving the validity of the current methodology.

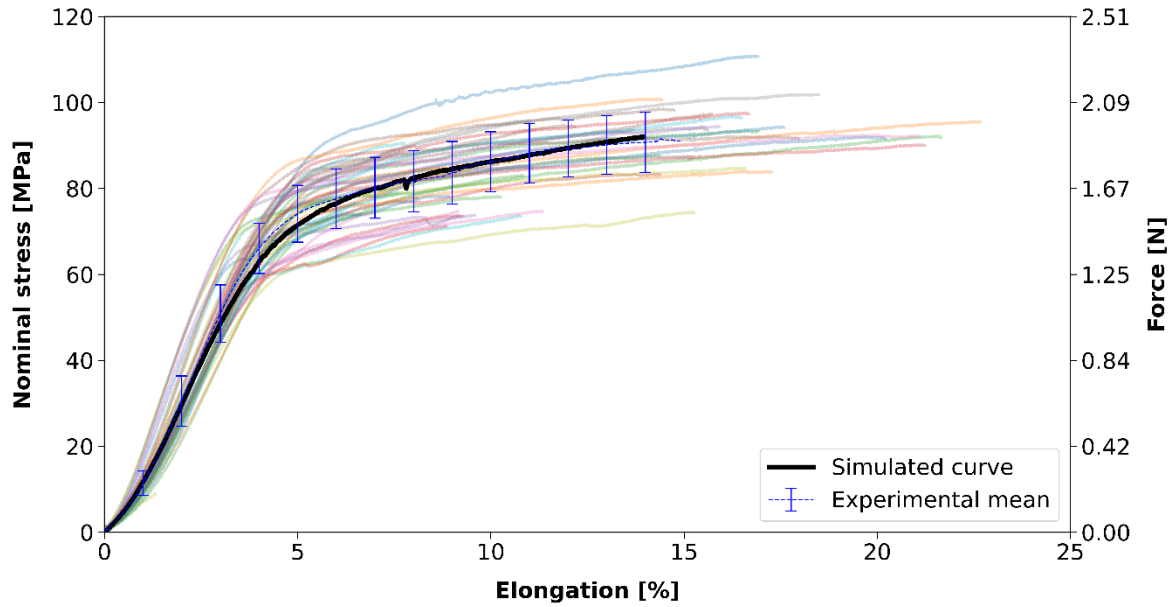

Figure 11 Comparison of the yarn's stress-strain curve obtained by simulation (in black) to the experimentally measured behavior (colored curves). The dashed blue curve shows the mean stress-strain curve from the experiments with error bars denoting the standard deviation. For each yarn that fails in the experiments (i.e. when the colored curve stops), the remaining sample size for the calculation of the mean and the standard deviation is reduced.

The strength of the current framework compared to pure experiments or theoretical structural models is illustrated in Figure 12 where the axial stress distribution along a fiber with a free end within the yarn core is shown. Insight into realistic stress distributions along single fibers and the internal microstructure is only possible by means of numerical simulations on high-fidelity geometrical yarn models.

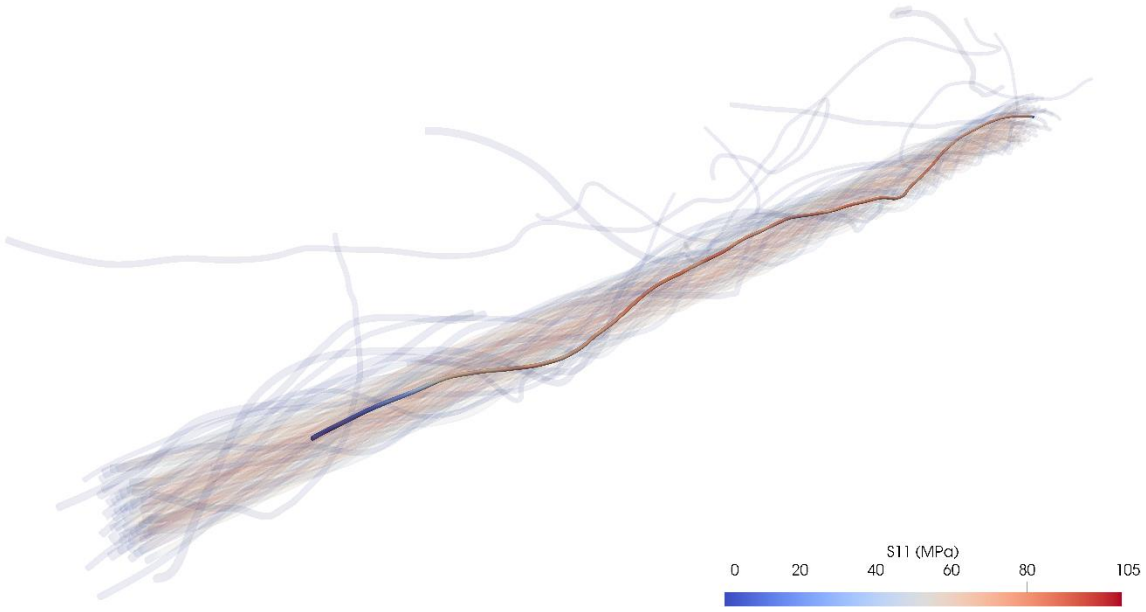

Figure 12 Axial stress distribution along the centerline of staple fiber with free end inside core (yarn elongation: 2.5 %)

Additionally, Figure 13 shows the axial stress distribution through a yarn cross-section at different levels of yarn elongation. From the top figure, it can be seen that for low yarn elongations, the axial fiber stress is highest in the center. This is linked to the fact that in the yarn core, the fibers are relatively straight and thus shorter per yarn unit length when compared to their neighbors at the circumference of the yarn. The latter have more room to straighten before taking up axial force as seen in the bottom figure, where it is clear that except for the fly-away fibers, the stress distribution is rather uniform through the cross-section at 10 % elongation. This relative uniform distribution is owing to the individual fiber stress-strain response. Indeed, for large strains, the stiffness –

represented by the high-deformation part of the material model in Abaqus – is small. Therefore, despite the possible large difference in strain between the central and outer fibers, the difference in stress is rather small.

It is clear from this figure that the fly-away fibers do not affect the mechanical response in the simulations. However, they affect the linear density of the yarn and therefore should be accounted for in the model when determining the yarn stress (normalized by tex).

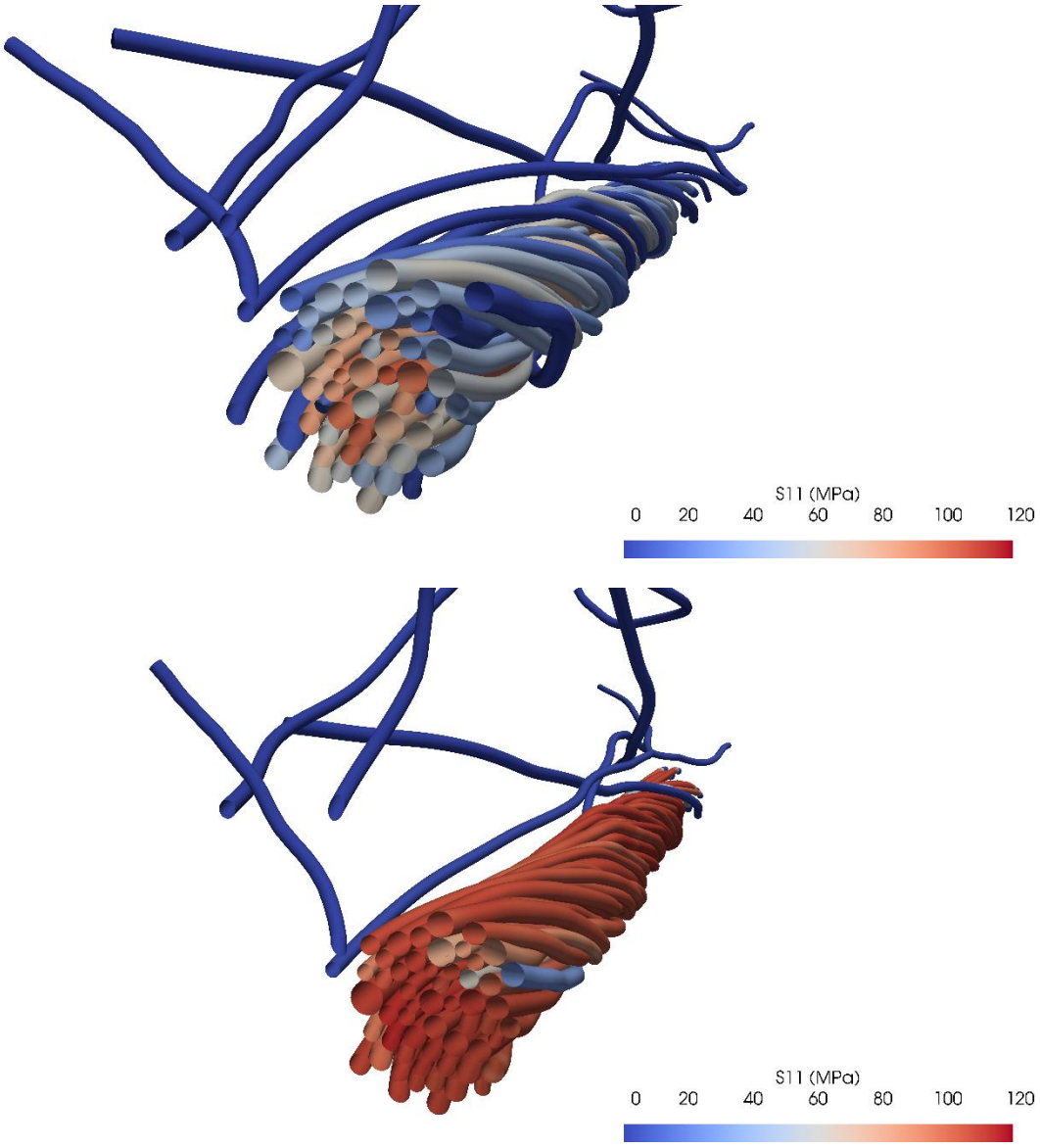

Figure 13 Axial stress distribution over a yarn cross-section for different yarn elongations (top: 2.5 % elongation, bottom: 10 % elongation). Section taken at 53 % of the yarn sample length.

To define the packing density, the yarn radial coordinate is subdivided into bins of equal spacing. The packing density in each bin then follows from the relative yarn area contoured by these bins that is occupied by fiber cross-sections. When looking at this parameter as a function of yarn elongation, shown in Figure 14, it is clear that the yarn core is not compacted anymore between 2.5 % and 10 % elongation. This does however not exclude internal reorganization at these moderate to high strains, especially at the yarn circumference and when fiber slippage occurs.

The computational cost for this tensile simulation is approximately 3.5 hours on 20 cores of a 2x20-core Intel Xeon Gold 6242R 3.1GHz machine.

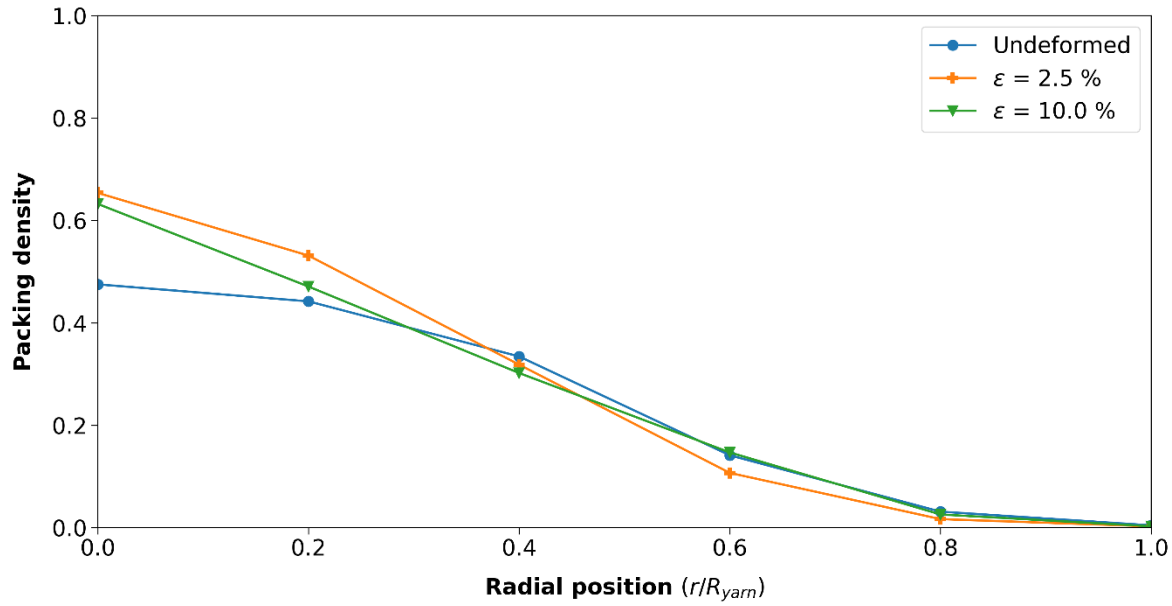

Figure 14 Yarn packing density as a function of relative radial position (w.r.t. undeformed yarn radius) for different yarn elongations.

To assess the validity of the numerical parameters chosen in the model setup, i.e. the element length, the damping factor, and the stable timestep size, as well as the yarn sample length, these parameters are altered and their influence on the slope of the simulated stress-strain curve is evaluated. The curve is approximated with a piecewise linear function and the slope of the elastic and plastic regime regions are compared.

Doubling the element length to 40 µm leads to a decrease in elastic stiffness of only 6.45 % and an increase in plastic stiffness of 4.21 %. However, increasing the element length leads to a more coarse approximation of the

smooth centerline curves, leading to more initial overlap between the fibers (63 overlapping elements instead of 11). Therefore, choosing an element length in the order of the average fiber diameter is reasonable.

When the mass-proportional Rayleigh damping is increased by a factor of 10, the stress-strain curves are distorted and an unphysical extra reaction force is measured. When this damping factor is decreased by a factor of 10, the elastic stiffness is $3.20\ \%$ smaller and the plastic stiffness increases by $2.33\ \%$, albeit with a more noisy appearance. The chosen damping factor is thus the maximal one that can be applied to obtain a smooth curve without introducing additional reaction forces.

Introducing mass scaling to increase the stable timestep size in Abaqus might lead to unwanted inertial effects. This is clearly observed when the stable timestep size is increased by a factor of 10 to 10^{-6} s. The stress-strain curve resembles a step function with constant nominal stress of 120 MPa reached within $1\ \%$ elongation. When the stable timestep size is reduced to 10^{-8} s (factor 10 smaller than the base case), the stress-strain curve is very similar to the one shown in Figure 11, with an elastic stiffness being $6.95\ \%$ lower and the curves becoming coincident at elongations larger than $10\ \%$. As a result, the chosen numerical parameters are conservative enough as to obtain physically representative results, yet allowing for a low computational cost.

Finally, also the effect of the yarn sample size is verified, to ensure that the sample in the scanner is of representative length. To this extent, three additional simulations are performed, one with $75\ \%$ of the sample length (starting from $z = 0$) and also simulations covering the upper and lower half of the yarn sample. As can be seen in Figure 15, the curves for the different samples are nearly coincident, with the largest difference in the transition zone between the two different linear regions. When one twist period of the yarn is considered as a unit cell, the proposed geometrical model is already significantly larger (2.5 twist periods). From this perspective, the geometrical model is certainly of representative length. Moreover, the boundary conditions were explicitly chosen such that the simulated sample is virtually part of a larger sample, as described in Section 2.3.1. However, when comparing the geometrical sample length (4.491 mm) to the average fiber length in the real-life yarn, which is in the order of centimeters, the simulated sample is rather short. This implies that the effect of fiber slippage in the tensile test is only accounted for to a limited extent. However, from Figure 12 it follows that the axial tension in the fiber builds up over a length smaller than 1 mm ($\approx 20\ \%$ of the sample length) close to the free end inside the yarn core. Behind this region, the tension is more or less uniform. Given this information, together with the observation that the simulated stress-strain curve of the yarn matches the experimentally measured stress-strain

curve, it is plausible that the fiber slippage effect is not very important for the tensile properties of this entire yarn. Insights about the importance of fiber slippage can only be obtained using realistic and detailed models as presented in this work.

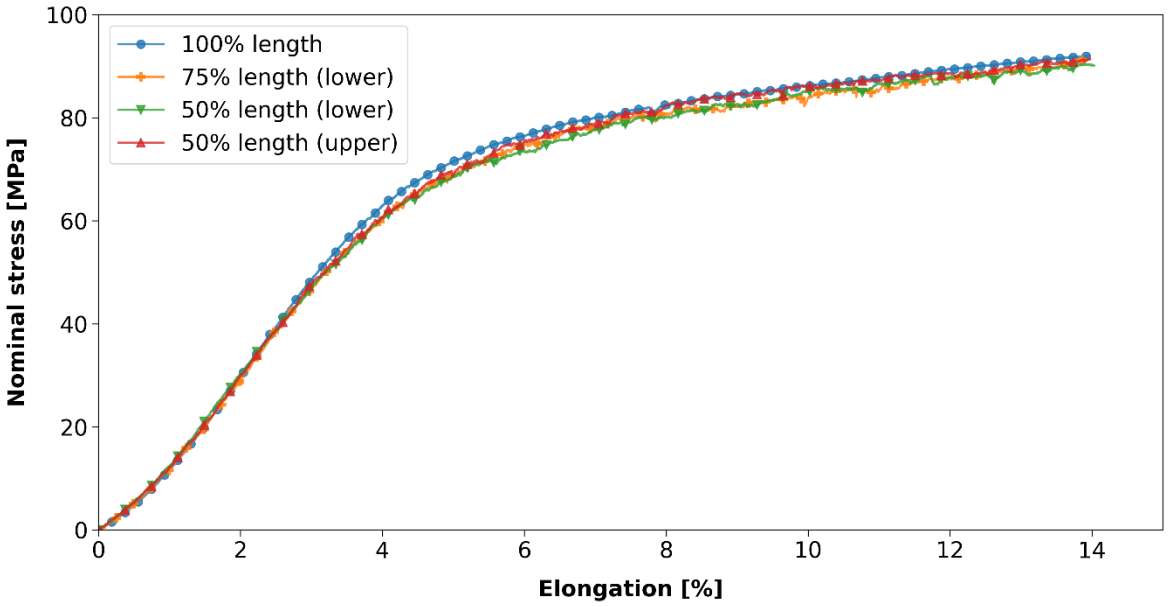

Figure 15 Stress-strain curves for different portions of the sample.

3.3 Simulating the Peirce cantilever test

To obtain the bending rigidity EI from the simulation, the following steps are performed. First, the deformation in the y-direction is obtained as a function of the original z-coordinate for all nodes. Subsequently, a curve is fitted to the data, similar to the procedure followed by Cornelissen and Akkerman[36]. The curve fit according to the Euler-Bernoulli beam theory is as follows:

$$y(z) = -\frac{w \cdot g}{24\,EI}(6L^2z^2 - 4Lz^3 + z^4) \tag{14}$$

Similarly, according to the Timoshenko beam theory, the following curve can be fitted to the data:

$$y(z) = -\frac{w \cdot g}{24\,EI}(6L^2z^2 - 4Lz^3 + z^4) - \frac{z}{k_y \cdot A \cdot G}\left(L - {}^{z}/_{2}\right) \tag{15}$$

Herein is y the lateral deformation, z the original axial coordinate, k_y the shear correction factor set to 0.89 for elements with circular cross-section[37], G the shear modulus and A the yarn cross section, inferred from the linear density. The only unknowns in these approximations are the bending stiffness EI and for the Timoshenko

approximation also the shear modulus G. The results are shown in Figure 16. The Euler-Bernoulli approximation yields a bending rigidity of $1.908 \cdot 10^{-9}$ Nm^2 (14.4 % lower than the experimentally measured rigidity) while the Timoshenko approximation leads to a bending rigidity of $1.915 \cdot 10^{-9}$ Nm^2 (-14.1 %) and a shear modulus of 3.68 GPa. When the yarn cross-sectional area inferred from the volumetric and linear densities is used as a measure for inertia, it follows that the ratio of shear modulus to Young's modulus in bending equals 61.7. Together with the observation that the yarn's end plane remains rather perpendicular to the yarn axis (see Figure 17), it can be concluded that the contribution of shear to the bending deformation is negligible, as also observed by Cornelissen and Akkerman[36]. The yarn's bending rigidity obtained by the Euler-Bernoulli curve fit relates to the fiber's bending rigidity EI_{fiber} ($2.882 \cdot 10^{-11}$ Nm^2, based on the average fiber diameter in the geometrical model) as $EI_{yarn} / EI_{fiber} = 66.2$, which nearly equals the number of fibers in the model.

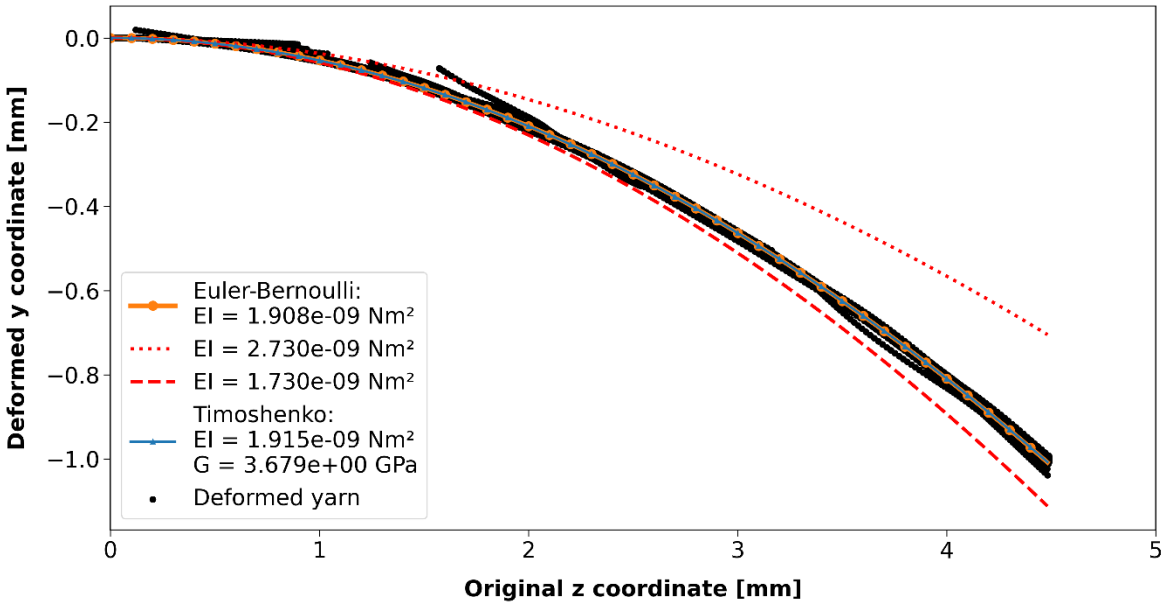

Figure 16 Yarn subjected to the Peirce cantilever test and the best curve fits of the Euler-Bernoulli and Timoshenko beam theories. Additionally, the dashed and dotted lines in red indicate the range of the experiments (average +/- standard deviation).

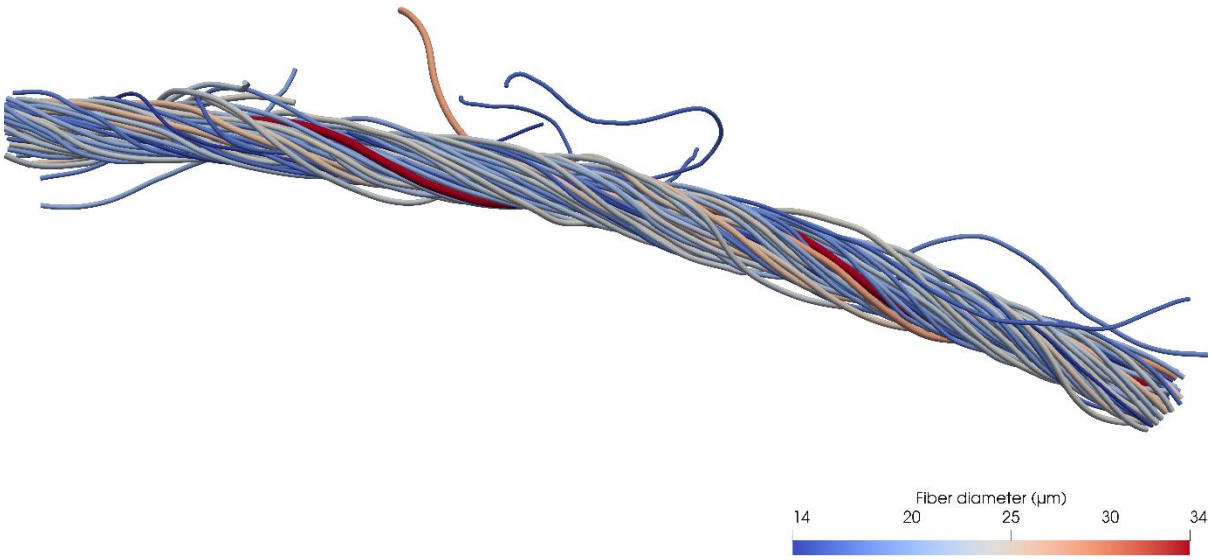

Figure 17 Deformed geometry at end of the bending simulation.

Finally, the curve fit of the Euler-Bernoulli equation can also be extrapolated until the average overhanging length L from the experiments is reached. The angle θ at $L = 40$ mm from the extrapolation is calculated to be 47.27°, which leads to an estimated bending rigidity EI of $1.748 \cdot 10^{-9}$ Nm^2 based on the Peirce cantilever equation, which is 21.6 % lower than the experimental average, albeit still within the measured range. The computational cost for this bending simulation is approximately 1.5 hours on 20 cores of a 2x20-core Intel Xeon Gold 6242R 3.1GHz machine.

Current simulation methodology allows to assess the influence of one single parameter, independently from the initial geometry. As an illustration of this capability, the yarn sample is untwisted with one revolution, corresponding to a reduction in twist of 2.23 revolutions/cm. Subsequently, the above experiment is repeated. In the rotation step, both yarn reference points are rotated in opposite direction with half a turn. The simulation time is set to 0.1 s and uniform mass scaling is added as to obtain a stable timestep size of 10^{-7}s. The kinematic coupling between fiber ends and yarn reference points is set such that only the radial direction is free and the yarn can thus contract or expand at its own will, similar to the tensile tests. No material damping is added. At the end of this simulation, the deformed geometry is extracted and serves as the base geometry for the bending step. As a result, this geometry is basically a new sample in an unstressed state, while the internal fiber arrangement of this sample is practically identical to the base geometrical model. The bending step has an identical setup as explained

in Section 2.3.2. The resulting curve fit to the Euler-Bernoulli beam equation yields a bending stiffness EI of $2.088 \cdot 10^{-9}$ Nm^2 (+9.43 % w.r.t. base case). It is apparent that for a decrease in yarn twist, the bending rigidity increases, as acknowledged by amongst others Dhingra and Postle[38] and Ly and Denby[39].

The procedure described above has the advantage that the influence of the twist on the yarn bending rigidity can be investigated independently from other parameters such as the base geometry or the internal stress state. Indeed, when two yarns with different twist levels are compared, the base geometry is different. Alternatively, in case the same yarn is tested twice but is untwisted before the second test, the test result will be influenced by the internal stresses originating from this untwisting unless the yarn is allowed to settle for a longer amount of time in a conditioned room. The numerical alternative allows to eliminate these influences to a maximal extent.

Finally, also the effect of the inter-fiber friction coefficient can be studied. In Section 2.3, a constant value of 0.25 was chosen for the inter-fiber friction coefficient, which is a simplification of reality. To verify its validity, two simulations were set up that alter the friction coefficient to half and double the original value, i.e. $\mu = 0.125$ and $\mu = 0.5$, respectively. The bending stiffness according to the formulation of Euler-Bernoulli beam theory for reduced friction equals $1.926 \cdot 10^{-9}$ Nm^2 (+0.94 % w.r.t. the base case) and for increased friction, EI was observed to be $1.916 \cdot 10^{-9}$ Nm^2 (+0.42 %). Surprisingly, altering the inter-fiber friction coefficient seems not to impact the bending stiffness significantly.

For frictional effects to be significant, there is of course a need for contact points. In the geometry extraction, the actual fiber diameter might be slightly underestimated. More importantly, the last stage of the centerline post-processing includes distance forcing between the fibers to avoid that they overlap, see Section 2.2.3. This leads to an underestimation of the actual contact points in the yarn. Finally, since the fibers are in a stress-free state at the beginning of the simulation, there is nothing that induces contact whereas in reality, there is some initial stress present due to winding and unwinding the yarn from the package and due to pushing the yarn on the Peirce test apparatus. Indeed, in the bending simulation, after 10^{-4} s only 10 nodes are registered to be in slipping contact, which equals 0.075 % of the mesh. In the tensile test, this effect is not much of an issue since the yarn is straightened, inducing yarn compaction and creating fiber contacts: after 5.6 ms, i.e. where the pretension of 0.5 cN/tex is reached, 28 % of the nodes are in contact.

This observation is important, as it seems that the bending stiffness of this yarn sample is mainly determined by the stiffness of the fibers themselves and that the contribution of friction is rather limited since the simulated

bending stiffness is well within the range of the experiments. As such, one could argue that a more advanced frictional model is of limited priority.

4 Conclusion

Established structural yarn models generally have good predictive abilities, but are often simplified in terms of geometry and sometimes fail to explain yarn behavior owing to the chaotic geometry. Other models represent the geometry in detail, but do not consider the yarn's structural behavior. Therefore, this paper develops new techniques to obtain a reliable structural model based on a geometry inferred from µCT scans. This allows for a better understanding of the deformations and stresses on the microscale level. Moreover, the influence of different structural parameters can be investigated for an identical geometry.

The validity of the resulting model has been assessed by comparing simulated tensile and bending tests to their experimental counterparts. The experimentally measured yarn behavior was reconstructed in an accurate manner using the developed model. Moreover, its versatility has been shown by altering individual parameters only. As such the effect of yarn twist and inter-fiber friction coefficient has been briefly touched upon in light of the Peirce cantilever test to determine the yarn's bending stiffness. It was found that reducing the yarn twist indeed increases the stiffness, but that altering the friction coefficient between the fibers has no significant effect. This observation is believed to be caused by the low number of nodes in contact in the geometrical model.

This work focuses on establishing a workflow for a single sample. As a result, the methodology is an important first step for statistical studies on multiple samples of the same yarn and toward homogenized macro-models for different yarns. In future work, more accurate material models could also be incorporated, as to simulate more complex yarn behavior, e.g. the hysteresis in cyclic loading. From the point of view of geometrical micromodels of the yarn, in the next step also fibers with a non-circular cross-section could be investigated, e.g. cotton fibers. It is expected that the proposed methodology remains valid as long as the scan resolution is sufficiently high, that is the contact region between fibers is smaller than the thickness of these fibers. In general, the proposed workflow stays the same, but some adaptations will be necessary to capture these particularities.

Declaration of Conflicting Interests

The authors declare that there is no conflict of interest.

Bibliography

1. Delcour L, Peeters J and Degroote J. Three-dimensional fluid-structure interaction simulations of a yarn subjected to the main nozzle flow of an air-jet weaving loom using a Chimera technique. *Textile Research Journal* 2020; 90: 194-212. DOI: 10.1177/0040517519862884.

2. Neckář B and Das D. Tensile Behavior of Staple Fiber Yarns Part I: Theoretical Models. *The Journal of The Textile Institute* 2017; 108: 922-930. DOI: 10.1080/00405000.2016.1204899.

3. Zubair M, Neckář B and Das D. Tensile Behavior of Staple Fiber Yarns Part II: Model Validation. *The Journal of The Textile Institute* 2017; 108: 931-934. DOI: 10.1080/00405000.2016.1204898.

4. Jiang XY, Hu JL and Postle R. A New Tensile Model for Rotor Spun Yarns. *Textile Research Journal* 2002; 72: 892-898. DOI: 10.1177/004051750207201007.

5. Liu T, Choi KF and Li Y. Mechanical Modeling of Singles Yarn. *Textile Research Journal* 2007; 77: 123-130. DOI: 10.1177/0040517507074022.

6. Park J-W and Oh A-G. Bending Rigidity of Yarns. *Textile Research Journal* 2006; 76: 478-485. DOI: 10.1177/0040517506063915.

7. Pan N. Development of a Constitutive Theory for Short Fiber Yarns: Mechanics of Staple Yarn Without Slippage Effect. *Textile Research Journal* 1992; 62: 749-765. DOI: 10.1177/004051759206201208.

8. Pan N. Development of a Constitutive Theory for Short Fiber Yarns Part II: Mechanics of Staple Yarn With Slippage Effect. *Textile Research Journal* 1993; 63: 504-514. DOI: 10.1177/004051759306300902.

9. Pan N. Development of a Constitutive Theory for Short Fiber Yarns Part III: Effects of Fiber Orientation and Bending Deformation. *Textile Research Journal* 1993; 63: 565-572. DOI: 10.1177/004051759306301002.

10. Van Langenhove L. Simulating the Mechanical Properties of a Yarn Based on the Properties and Arrangement of its Fibers Part I: The Finite Element Model. *Textile Research Journal* 1997; 67: 263-268. DOI: 10.1177/004051759706700405.

11. Van Langenhove L. Simulating the Mechanical Properties of a Yarn Based on the Properties and Arrangement of its Fibers Part II: Results of Simulations. *Textile Research Journal* 1997; 67: 342-347. DOI: 10.1177/004051759706700506.

12. Van Langenhove L. Simulating the Mechanical Properties of a Yarn Based on the Properties and Arrangement of its Fibers: Part III: Practical Measurements. *Textile Research Journal* 1997; 67: 406-412. DOI: 10.1177/004051759706700604.

13. Sriprateep K. CAD/CAE for stress–strain properties of a wide range of multifilament twisted man-made filament yarns. *Textile Research Journal* 2019; 89: 204-215. DOI: 10.1177/0040517517741162.

14. Sriprateep K and Bohez ELJ. CAD/CAE for stress–strain properties of multifilament twisted yarns. *Textile Research Journal* 2017; 87: 657-668. DOI: 10.1177/0040517516636000.

15. Vassiliadis S, Kallivretaki A and Provatidis C. Mechanical modelling of multifilament twisted yarns. *Fibers and Polymers* 2010; 11: 89-96. DOI: 10.1007/s12221-010-0089-6.

16. Wang Y and Sun X. Digital-element simulation of textile processes. *Composites Science and Technology* 2001; 61: 311-319. DOI: https://doi.org/10.1016/S0266-3538(00)00223-2.

17. del Sorbo P, Girardot J, Dau F, et al. Numerical investigations on a yarn structure at the microscale towards scale transition. *Composite Structures* 2018; 183: 489-498. DOI: https://doi.org/10.1016/j.compstruct.2017.05.018.

18. Daelemans L, Dinh TD and Van Paepegem W. Virtual fiber modelling: a viable multi-scale approach for mechanical modelling of textile materials. In: *SAMPE Europe 2020 Conference* 2020.

19. Daelemans L, Faes J, Allaoui S, et al. Finite element simulation of the woven geometry and mechanical behaviour of a 3D woven dry fabric under tensile and shear loading using the digital element method. *Composites Science and Technology* 2016; 137: 177-187. DOI: https://doi.org/10.1016/j.compscitech.2016.11.003.

20. Daelemans L, Tomme B, Caglar B, et al. Kinematic and mechanical response of dry woven fabrics in through-thickness compression: Virtual fiber modeling with mesh overlay technique and experimental validation. *Composites Science and Technology* 2021; 207: 108706. DOI: https://doi.org/10.1016/j.compscitech.2021.108706.

21. Sriprateep K and Bohez EL. Computer Aided Modeling of Fiber Assemblies. *Computer-Aided Design and Applications* 2006; 3: 367-376. DOI: 10.1080/16864360.2006.10738475.

22. Sriprateep K and Bohez EL. A new computer geometric modelling approach of yarn structures for the conventional ring spinning process. *The Journal of The Textile Institute* 2009; 100: 223-236. DOI: 10.1080/00405000701757958.

23. Schröder K, Zinke A and Klein R. Image-Based Reverse Engineering and Visual Prototyping of Woven Cloth. *IEEE Transactions on Visualization and Computer Graphics* 2015; 21: 188-200. DOI: 10.1109/TVCG.2014.2339831.

24. Zhao S, Luan F and Bala K. Fitting Procedural Yarn Models for Realistic Cloth Rendering. In: *ACM Transactions on Graphics* 2016, pp.1-11.

25. Gaiselmann G, Manke I, Lehnert W, et al. Extraction of Curved Fibers from 3D Data. *Image Analysis & Stereology* 2013; 32: 57-63. DOI: 10.5566/ias.v32.p57-63.

26. Huang X, Wen D, Zhao Y, et al. Skeleton-based tracing of curved fibers from 3D X-ray microtomographic imaging. *Results in Physics* 2016; 6: 170-177. DOI: 10.1016/j.rinp.2016.03.008.

27. Henyš P and Čapek L. Individual yarn fibre extraction from micro-CT: multilevel machine learning approach. *The Journal of The Textile Institute* 2021; 112: 1979-1985. DOI: 10.1080/00405000.2020.1865503.

28. Peirce FT. The "handle" of cloth as a measurable quantity. *Journal of the Textile Institute Transactions* 1930; 21: T377-T416. DOI: 10.1080/19447023008661529.

29. Lammens N, Kersemans M, Luyckx G, et al. Improved accuracy in the determination of flexural rigidity of textile fabrics by the Peirce cantilever test (ASTM D1388). *Textile Research Journal* 2014; 84: 1307-1314. DOI: 10.1177/0040517514523182.

30. Lee TC, Kashyap RL and Chu CN. Building Skeleton Models via 3-D Medial Surface Axis Thinning Algorithms. *CVGIP: Graphical Models and Image Processing* 1994; 56: 462-478. DOI: https://doi.org/10.1006/cgip.1994.1042.

31. Otsu N. A Threshold Selection Method from Gray-Level Histograms. *IEEE Transactions on Systems, Man, and Cybernetics* 1979; 9: 62-66. DOI: 10.1109/TSMC.1979.4310076.

32. Nützi G. Worm Analysis, https://github.com/gabyx/WormAnalysis/blob/master/SkeletonTest/Skeletonize.ipynb (2017, 2022).

33. Bloomenthal J and Rokne J. Homogeneous coordinates. *The Visual Computer* 1994; 11: 15-26. DOI: 10.1007/BF01900696.

34. Blackman R and Tukey J. *The measurement of power spectra*. New York: Dover Publications, 1958.

35. Hearle JWS. 4 - Physical properties of wool. In: Simpson WS and Crawshaw GH (eds) *Wool: Science and Technology*. Woodhead Publishing, 2002, pp.80-129.

36. Cornelissen B and Akkerman R. Analysis of yarn bending behaviour. In: *17th International Confence on Composite Materials (ICCM)* 2009, p.10.

37. Cowper R. The Shear Coefficient in Timoshenko's Beam Theory. *Journal of Applied Mechanics* 1966; 33: 335-340.

38. Dhingra RC and Postle R. The bending and recovery properties of continuous-filament and staple-fibre yarns. *The Journal of The Textile Institute* 1976; 67: 426-433. DOI: 10.1080/00405007608630161.

39. Ly NG and Denby EF. Bending Rigidity and Hysteresis of Wool Worsted Yarn. *Textile Research Journal* 1984; 54: 180-187. DOI: 10.1177/004051758405400307.